Journal of Marine Systems 178 (2018) 29–37

Contents lists available at ScienceDirect

Journal of Marine Systems

journal homepage: www.elsevier.com/locate/jmarsys

Coastal upwelling south of Madagascar: Temporal and spatial variability

Juliano D. Ramanantsoa[a,e,*], M. Krug[a,b,c], P. Penven[d], M. Rouault[a,c], J. Gula[d]

[a] Department of Oceanography, University of Cape Town, South Africa
[b] Council for Scientific and Industrial Research, Cape Town, South Africa
[c] Nansen Tutu for Marine Environmental Research, South Africa
[d] Univ. Brest, CNRS, IRD, Ifremer, Laboratoire d'Océanographie Physique et Spatiale, IUEM, Brest, France
[e] Institut Halieutique et des Sciences Marines, Toliara, Madagascar

ARTICLE INFO

Keywords:
Coastal upwelling
South of Madagascar
Ekman transport
East Madagascar Current
Sea Surface Temperature
Numerical model

ABSTRACT

Madagascar's southern coastal marine zone is a region of high biological productivity which supports a wide range of marine ecosystems, including fisheries. This high biological productivity is attributed to coastal upwelling. This paper provides new insights on the structure, variability and drivers of the coastal upwelling south of Madagascar. Satellite remote sensing is used to characterize the spatial extent and strength of the coastal upwelling. A front detection algorithm is applied to thirteen years of Multi-scale Ultra-high Resolution (MUR) Sea Surface Temperatures (SST) and an upwelling index is calculated. The influence of winds and ocean currents as drivers of the upwelling is investigated using satellite, in-situ observations, and a numerical model. Results reveal the presence of two well-defined upwelling cells. The first cell (Core 1) is located in the southeastern corner of Madagascar, and the second cell (Core 2) is west of the southern tip of Madagascar. These two cores are characterized by different seasonal variability, different intensities, different upwelled water mass origins, and distinct forcing mechanisms. Core 1 is associated with a dynamical upwelling forced by the detachment of the East Madagascar Current (EMC), which is reinforced by upwelling favourable winds. Core 2 appears to be primarily forced by upwelling favourable winds, but is also influenced by a poleward eastern boundary flow coming from the Mozambique Channel. The intrusion of Mozambique Channel warm waters could result in an asynchronicity in seasonality between upwelling surface signature and upwelling favourables winds.

1. Introduction

The marine coastal regions south of Madagascar are highly productive (Bemiasa, 2009; Pripp et al., 2014). Biological production in these coastal regions is driven by an active coastal upwelling, which boosts coastal ocean fertilization. Several local biological studies have further confirmed that the coastal upwelling south of Madagascar is a hotspot of marine biological productivity (Houart and Héros, 2013); (Rakotoarinivo, 1998). Satellite observation of Sea Surface Temperature (SST) and Chlorophyll A concentration can be used to identify upwelling regions south of Madagascar as shown in Fig. 1. In that synoptic map, cold waters near the coast associated with high Chlorophyll A concentrations are indicative of a coastal upwelling event. A better understanding of upwelling variability south of Madagascar is essential to adequately manage and preserve these ecologically and economically important coastal regions (Bemiasa, 2009). Coastal upwelling south of Madagascar may also impact productivity over the larger south Indian Ocean. The region south-east of Madagascar and within the Southern Indian Ocean Counter Current (Siedler et al., 2009) is subject to one of the largest chlorophyll blooms observed in the open ocean (Longhurst, 2001; Wilson and Qiu, 2008). The formation, propagation and termination of this bloom remain a topic of active research (Srokosz et al., 2015), but several studies point to a possible link between the coastal upwelling regions of Madagascar and the large bloom of phytoplankton spreading in the south Indian Ocean (Huhn et al., 2012; Srokosz and Quartly, 2013). Consequently there is a strong need to adequately characterise and understand the mechanisms which drive this upwelling.

Limited studies have addressed the seasonality and variability of the coastal upwelling south of Madagascar. Ho et al. (2004) were the first to investigate its seasonality. Their work was based on an analysis of observations of chlorophyll A concentrations derived from the SeaWiFs sensor over the period 1997–2001. They showed that upwelling along the South Madagascar coastline was greater during the austral winter (May–Oct) than in the austral summer (Nov–Apr) months. A later study by Raj et al. (2010) further suggested that shallower mixed layer during summer season tended to promote the summer upwelling.

Coastal upwelling south of Madagascar is thought to be driven by

* Corresponding author at: Department of Oceanography, University of Cape Town, Office 123, Private Bag X3, Rondebosch Cape Town 7701, South Africa.
E-mail address: oceanman1@live.fr (J.D. Ramanantsoa).

http://dx.doi.org/10.1016/j.jmarsys.2017.10.005
Received 5 June 2017; Received in revised form 20 October 2017; Accepted 20 October 2017
Available online 26 October 2017

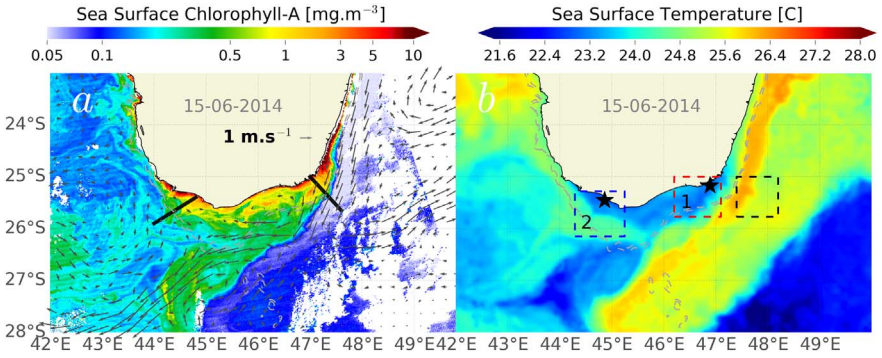

Fig. 1. Correspondence between inshore cold water and chlorophyll A concentration response. (a) Map of sea surface chlorophyll A concentration on the 15/06/2014 south of Madagascar. The black arrows represent the geostrophic current. Black lines are transects taken inside respective upwelling cells. (b) Sea surface temperature on the same day. Black stars are the position where the Lagrangian particles are released. The boxes are the relevant location for computing the sea surface temperature-based Coastal Upwelling Index. The red box (numbered 1) will represent upwelling cell Core 1, the blue box (numbered 2) will represent upwelling cell Core 2 and the black box will represent the offshore temperature. Dashed contour lines are the isobaths at 500 m and 1000 m depth.

coastal winds (DiMarco et al., 2000) and/or interactions between the East Madagascar Current (EMC) and the shelf (Lutjeharms and Machu, 2000). DiMarco et al. (2000) argued that wind stress in austral summer favors upwelling events. However, Lutjeharms and Machu (2000) did not find a significant correlation between the wind and the presence of upwelled water near the coast. Instead, Machu et al. (2002) suggested that the formation of cyclonic eddies through interactions between the EMC and the continental shelf could influence the strength of the upwelling. Ho et al. (2004) also showed a link between upwelling and the EMC. The influence of the EMC on the coastal upwelling was later confirmed by the idealized modeling work of Jose et al. (2016) which illustrates the potential effects of the detachment of the EMC on vertical velocities.

This paper seeks to provide an improved understanding of the spatial extent and seasonal variability of the upwelling south of Madagascar and clarify its complex generating mechanisms. For that purpose, we use satellite observations and outputs from an ocean numerical model.

Section 2 describes the observations, model and techniques used in this study. Section 3 presents the characteristics of the upwelling cells, their extents, and their seasonal variations. Section 4 addresses the relative role of the wind and the ocean currents as drivers of the coastal upwelling. A discussion and conclusions are presented in Section 5.

2. Data, model and method

2.1. Observation

Table 1 details the dataset used in this study. The Multi-Scale Ultra-High Resolution (MUR) SST is a gridded, blended, and gap-free dataset developed by NASA-JPL. It is produced by merging data from MODIS, AMSR-E, WINDSAT, and AVHRR on a 0.011° grid and it combines the capacity of high-resolution infrared waveband and the signal-crossing atmosphere by microwaves waveband (Vazquez-Cuervo et al., 2013). Vazquez-Cuervo et al. (2013) showed that the MUR SST product is well suited to the study of coastal upwelling processes. Since we are focusing on the seasonal cycle, we use monthly data calculated from daily data. Comparisons between the MUR SST and the MODIS level 2b SST (pure infrared but highly limited by atmospheric contamination) show that both mean SST are strongly correlated inside the upwelling region during period of 2003 to 2015 with a correlation factor of 0.992 significant at the 0.95 level. Wind fields observed from the Advanced Scatterometer dataset (ASCAT METOP-A) [Table 1] were used. The ASCAT sensor is less prone to rain and land contamination (Hilburn et al., 2006) and therefore well suited for coastal regions. This wind product is operationally monitored and processed through EUMETSAT (Hasager et al., 2015).

The Moderate-Resolution Imaging Spectroradiometer (MODIS) chlorophyll A was downloaded from the NASA Ocean Color Nasa website and processed by the Marine Remote Sensing Unit (MSRU, Cape Town, South Africa). Monthly composites of Chlorophyll A concentrations are derived from the 1 km gridded L3 Aqua and TERRA MODIS daily maps.

The GlobCurrent product is a combination of geostrophic currents from satellite altimetry and Ekman currents calculated from ECMWF ERA INTERIM reanalysis winds (Johannessen et al., 2015). The GlobCurrent data are provided at a 3-hourly frequency, and on a $\frac{1}{4}^{\circ}$ resolution grid. They are combined as monthly composites for this study.

We also used a 2.5-year time series (10/2010 to 02/2013) of the EMC volume transport to investigate the relationship between EMC and upwelling intensity. The EMC transport data were derived from Acoustic Doppler Current Profiler (ADCP) observations collected across the EMC at a latitude of 23°S. The dataset provided by the NIOZ (Royal Netherlands Institute for Sea Research), was collected during the INATEX research project (Ponsoni et al., 2016).

2.2. Model setup and Lagrangian experiment

To investigate the physical drivers of the upwelling, we analyzed outputs from a regional ocean model and performed additional numerical sensitivity studies. We used the outputs of a nested configuration of the Coastal and Regional Ocean Community model (CROCO), which is an evolution of the ROMS_AGRIF model (Debreu et al., 2012; Shchepetkin and McWilliams, 2005). The model simulates the ocean circulation around the African continent including Madagascar, over 23 years (1990–2013), using a $\frac{1}{12}^{\circ}$ resolution nested grid. The model surface conditions are derived from the ERA Interim atmospheric reanalysis (Dee et al., 2011) using a bulk formulation (Fairall et al., 1996). The lateral boundary conditions are forced by the GLORIS ocean reanalysis (Ferry et al., 2012). The model outputs were compared with

Table 1
Data sets and their sources. The first column lists the data source and the sensor (when applicable, in parentheses), the second column is the variable measured or estimated, the third column is the temporal resolution, the fourth column the spatial resolution (in degree), the fifth column the data record length, and the sixth column the Internet resource from which the data were downloaded.

Data source (sensor)	Variable	Composite	Resolution grid	Period	URL
Aqua (MODIS)	Chlorophyll A	Monthly	1/100 ^{o}	2003–2015	http://www.afro-sea.org.za/
MUR	SST	Monthly	1/100 ^{o}	2003–2015	http://mur.jpl.nasa.gov/
MetOp-A (ASCAT)	Wind	Monthly	1/4 ^{o}	2009–2015	http://www.ifremer.fr/cersat/en/data/data.html/
GlobCurrent	Surface currents	Monthly	1/4 ^{o}	2003–2015	http://www.ifremer.fr/opendap/cerdap1/globcurrent/

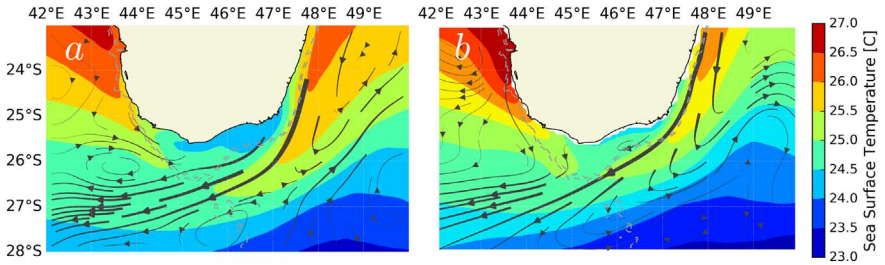

Fig. 2. Comparison between observation dataset and model outputs. (a) Average of MUR SST, and streamlines of mean ocean velocity from GlobCurrent over the period 2003-2015. (b) Mean SST and streamlines of mean ocean velocity from the model over the period 1993–2013.

satellite observations (Fig. 2). The main characteristics of the upwelling are well reproduced in the model.

The influence of the coastal circulation is investigated by tracking the origin of the water masses that feed into the coastal upwelling cells through a Lagrangian particle tracking experiment applied to the model outputs. To define major pathways of upwelled water, three-dimensional velocity fields are used to advect the particles of water backward in time over a two-month period. Particles are advected using the code described in Gula et al. (2014). Particles are released at the two locations shown as black stars in Fig. 1. The particles are released every 5 m in the upper 50 m. 168 particles are released in a first upwelling cell (46.8°E–47.2°E; 25.1°S–25.5°S) (Core 1: southeast of Madagascar; Fig. 1) and 126 in a second cell (44.7°E–45.1°E; 25.45°S–25.85°S) (Core 2: southern tip of Madagascar; Fig. 1) every year from 2003 to 2013.

In addition, a second model configuration is used for idealized simulations. The model has a $\frac{1}{12}^{\circ}$ grid resolution similar to the first configuration. It is forced by a QuickScat wind stress climatology and the boundary conditions are constructed from the World Ocean Atlas (Conkright et al., 2002). The model is able to reproduce the coastal upwelling. These idealized simulations are used to perform sensitivity studies and investigate the role of the wind stress, the EMC, and the coastal circulation as drivers of the coastal upwelling.

2.3. Upwelling frontal detection

A front detection algorithm is applied to monthly SST maps to identify surface temperature fronts south of Madagascar. The method proposed here is an adaptive Canny edge detector applied on multiple images (Canny, 1986). Each monthly SST composite map is preliminarily low-passed filtered using a Gaussian filter with a sigma value of 1 (Higdon, 1998), to omit small scale variability. A Sobel operator with a fixed 3×3 window is then used to highlight the regions associated with the strongest SST fronts in the monthly images (Simhadri et al., 1998; Ping et al., 2016). Following that step, only the strongest gradients in a 3×3 window and along both an East-West and North-South axis are selected (Othman et al., 2012). Afterwards, the monthly upwelling fronts are defined as frontal regions tracked from a range of optimal thresholds of SST gradient following the formula in Othman et al. (2012), $T_{low} = \frac{1}{2}T_{high}$, where T_{low} is average lower gradient and T_{high} is the optimal higher gradient in our case falling with a range of 0.76 °C.km^{-1} and 1.51 °C.km^{-1}. Lastly, all monthly frontal maps are combined seasonally to identify only the zones with a high number of frontal occurrences.

2.4. Upwelling spatial extent

The spatial extent of the upwelling cell is estimated by following a surface isotherm encompassing the colder coastal upwelled waters. The value of isotherm used is calculated following Veitch et al. (2010), according to Eq. (1).

$$SST_{upwelling} = 0.25SST_{coast} + 0.75SST_{offshore} \quad (1)$$

where SST_{coast} [°C] is the lowest SST inside the upwelling zone located over the shelf south of Madagascar, and $SST_{offshore}$ [°C] is taken off the southern tip of Madagascar in the vicinity of the 1000 m isobath, averaged over the longitudes 45°E, 46°E and latitudes 26°S, 27°S.

2.5. Upwelling index

We computed a SST-based Coastal Upwelling Index (CUI) adapted from Demarq and Faure (2000) method:

$$CUI = \frac{SST_{offshore} - SST_{coast}}{SST_{offshore} - SST_{mean}} \quad (2)$$

Where $SST_{offshore}$ is the mean warm SST inside the black box in Fig. 1, SST_{coast} is the mean SST in red or blue box in Fig. 1, and SST_{mean} is the temporal average of SST_{coast}. The SST difference is taken between the monthly temperature in the coastal zone (SST_{coast}) for each upwelling cell (red box or blue box in Fig. 1) and the offshore temperature ($SST_{offshore}$) at the same latitude inside the core of the EMC (black box in Fig. 1) using a similar approach to that described in Benazzouz et al. (2014). The box chosen to derive $SST_{offshore}$ is adapted to account for the influence of the EMC on coastal upwelling (Lutjeharms and Machu, 2000; DiMarco et al., 2000; Ho et al., 2004). This difference is normalized by dividing by the difference between $SST_{offshore}$ and the temperature averaged in time over both coastal boxes (SST_{mean}) to account for seasonal solar heating as described by Alvarez et al. (2011) and Gonzalez-Nuevo et al. (2014). The CUI ranged from a value of 0 (no upwelling) to values greater than 1 which are indicative of strong upwelling.

2.6. Cross shore Ekman transport

To test the influence of winds on coastal upwelling, we estimate the cross shore Ekman transport (CSET) following the methods described by Bakun (1975). The cross shore Ekman transport is derived using the component of the wind stress parallel to the coast.

$$\tau_{alonshore} = C_d \rho_a V^2 (\beta - \alpha) \quad (3)$$

$$CSET = \frac{\tau_{alongshore}}{\rho_o f} \quad (4)$$

Where, $\tau_{alongshore}$ [$m^2.s^{-1}$] is the along shore wind stress, ρ_a [$kg.m^{-3}$] is the density of air at 10 m above the water surface, Cd is the dimensionless drag coefficient following Large and Pond (1981), V [$m.s^{-1}$] is the 10 m wind speed, α is the wind direction, β is the dominant coastline angle (azimuth), ρ_o [$kg.m^{-3}$] is the density of water, and f is the Coriolis parameter.

3. Characteristics, extent, and seasonal variations of the upwelling cells

3.1. Spatial patterns of cold coastal temperature

The mean SST over the period 2003-2015 shows the presence of colder water close to the coast south of Madagascar (Fig. 3a). This upwelled water lies over the shelf between the 0 m and the 500 m isobaths with the lowest temperatures near the shore. On average, this upwelled water is 1.65 °C colder than the waters offshore. The

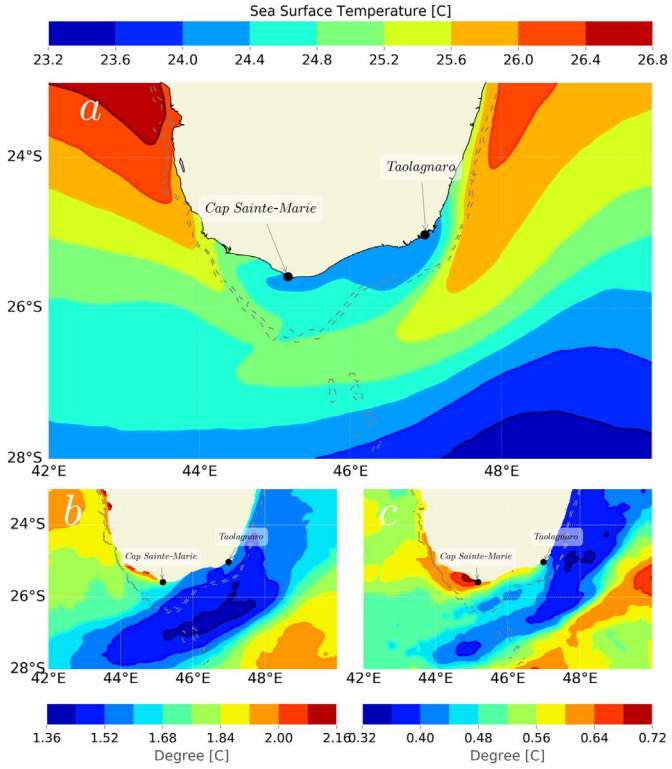

Fig. 3. (a) Mean SST for 2003–2015 using MUR SST product which reflects the strong signature of inshore cold water, marker of coastal upwelling, south of Madagascar. Grey dotted lines are isobaths at 500 m and 1000 m. (b) Root Mean Square (RMS) of the annual SST variation. (c) Root Mean Square (RMS) of the interannual SST anomaly for 2003–2015.

upwelling extends from 24.4°S along the south-east coast, north of Taolagnaro (also called Fort Dauphin), to Cap Sainte-Marie (25.6°S), the southernmost point in Madagascar (Fig. 3.a). The transition between the cold upwelled water and the offshore warm water is sharp. The offshore warm water is transported by the EMC from the east, and another warm water appearing to be a surface current extends from the Mozambique Channel to the western side of Madagascar (Fig. 3.a). The transition between cold and warm waters is more gradual in the southern part of the shelf, probably due to an important eddy variability there (Halo et al., 2014).

Fig. 3.b shows the root mean square (RMS) of the annual SST cycle. Warm surface waters associated with the EMC display less variability (1.45°C RMS) than those located further west where RMS values range from 1.7 to 2.1°C (Fig. 3.b). The largest RMS values of 2.1°C are encountered in the southwestern coastal regions located closest to the Mozambique channel. In comparisons, the SST RMS near Taolagnaro is of the same order of magnitude as is SST RMS within the neighbouring EMC waters.

The inter-annual SST RMS based on SST anomalies is shown in Fig. 3.c. Again, the inter-annual variability in the western coastal upwelling regions, off Cap Sainte-Marie, is higher. These upwelling regions are associated with inter-annual RMS values of 0.72°C. On the southeastern side, the upwelling coastal regions and the EMC both display low inter-annual variability with a RMS value of 0.40°C. These results suggest the presence of two distinct cold water bodies with different annual and inter-annual levels of variability: Core 1, in the southeastern corner of Madagascar, and Core 2, west of the southern tip of Madagascar. The variability of Core 1 is weaker due to the influence of the EMC.

Fig. 4 shows the spatial distribution of the monthly occurrence of cold water events detected within the entire study region (43°E–48°E; 24°S–26.5°S). Coldest waters in the monthly dataset occur in two

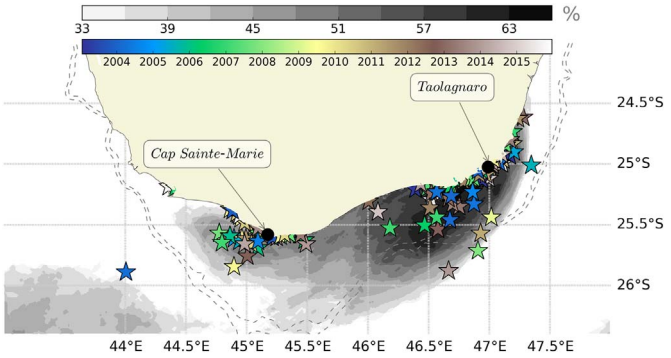

Fig. 4. Spatial distribution of the lowest temperature. Stars represent the lowest temperature each month over the period 2003–2015 taken for the whole upwelling region. The occurrence of cold water (in %) over the same period, is shown in grey scales.

distinct locations. The first location (Core 1), lies in the south-east corner of Madagascar close to Taolagnaro, around 47°E and 25°S. Our analysis shows a fairly wide and scattered spatial distribution for these cold pockets of waters which encompasses the region of cold mean SST seen in Fig. 3a. It is located at the inshore edge of the detached EMC, where a well-defined minimum of temperature can be observed throughout the year. The second region where cold waters occur is found at the south-west corner of Madagascar, in the vicinity of 45°E, where Core 2 is located. The spatial distribution of coldest water events in this region shows less scatter and a more coherent grouping and is coincident with the location of the mean colder water features in Fig. 3a. These findings confirm that upwelling South of Madagascar, identified through the analysis of both mean and minimum surface water temperature values, occurs within 2 different cells: Core 1 and Core 2. The Core 1 is subjected to a high spatial spread and a high amount of upwelled water than in Core 2 (Fig. 4), which is explained by the perennial behaviour of Core 1, unlike Core 2 which is subjected to high variabilities (Fig. 3b.c).

The definition of a SST minima associated with two upwelling cores allows the computation of the percentage occurrence of colder water between 2003 and 2015 according to Eq. (1). Fig. 4 shows that upwelling occurs in Core 1 almost 70% of the time, illustrating its permanent nature. The maximum value is about 50% for Core 2, in agreement with the higher variability seen in Fig. 3.

3.2. Seasonal extensions of the upwelling cells

The aim of this section is to highlight the seasonal characteristics of the two cores. To better identify regional variations in upwelling strength and spatial extent, we identify SST fronts with the frontal detection algorithm described in Section 2.3. Fig. 5 presents the occurrence of SST fronts between 2003 and 2015. These SST fronts delineate the borders of the two upwelling cores for each season. SST fronts are present all year long, east and west of Core 1, and on the southern part of the shelf, inshore of the EMC. SST fronts are also detected around Core 2 in Summer (JFM), Fall (AMJ) and Winter (JAS). This confirms the presence of two well-defined upwelling cores on the eastern and western part of the upwelling. The eastern boundary of Core 1 is quite spatially invariant throughout the year. It extends from the east coast to the southern tip of Madagascar, following the shelf break between the 1000 m and the 2000 m isobaths. However, the southern extension of Core 1 is more seasonally variable, being more defined in fall and winter and less evident in Spring (OND). The western boundary of Core 2 is distinguishable in summer, fall and winter (Fig. 5). It starts from the southwestern corner of Madagascar at 25°S, and follows the shelf along the 1000 m isobath and in a southeastern direction. Another front can be observed south of Madagascar between the two cores (for example at 45°E in Winter, Fig. 5c), highlighting their different water characteristics and behaviour. The result emphasizes

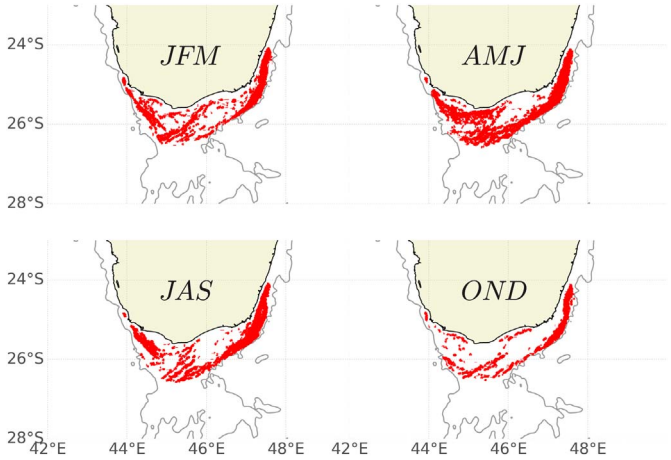

Fig. 5. Seasonal distribution of coastal upwelling fronts based on SST. Red lines are SST fronts detected over the period 2003–2015, based on multiple image canny edge detection method. Grey lines are 2000 m isobath.

that Core 1 is almost permanent throughout the year but is more intense in autumn and winter. Core 2 is present for the first three seasons of the year but less visible in spring.

Now that we have identified two distinct upwelling cores, we will characterize the differences between these two cores and focus on upwelling intensities.

3.3. Seasonal variations of core intensity

Fig. 6 presents the monthly climatology of the upwelling index (CUI) based on SST, presented in Section 2.5, for the upwelling cells in Core 1 (red bold line) and Core 2 (blue bold line). It also shows the seasonal variations in chlorophyll A concentration and offshore Ekman transport. The variability of the CUI is dominated by a seasonal cycle with a maximum in winter for the two cores. In agreement with the results presented in the previous section, CUI variations show that upwelling is present throughout the year in Core 1. For Core 2, although the CUI also reaches a value of about 0.5 in winter, it is much weaker with almost no upwelling from October to January. While temperature differences across an upwelling front are not necessarily linked to upwelling (Gunther, 1936; Oram et al., 2008), several characteristics of Core 2 point to the occurrence of active upwelling. Between October and January, surface waters in Core 2 are still generally colder than those of neighbouring waters but the spatial extent of Core 2 decreases. The high variability which characterises Core 2 which at times masks the upwelling, is probably caused by the wider range of mechanisms

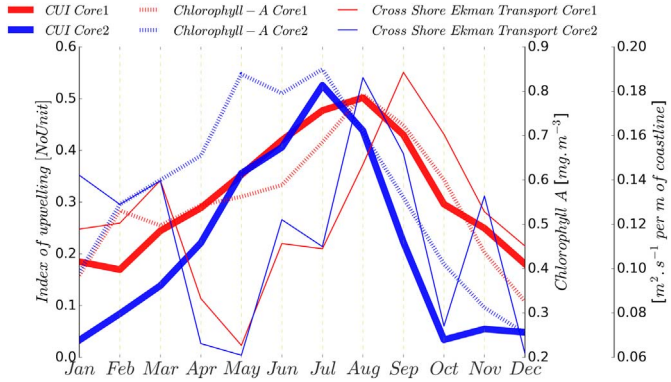

Fig. 6. Bold solid lines are seasonal variation of coastal upwelling index. Dotted lines are seasonal variation of chlorophyll A concentration ($mg.m^{-3}$). Solid lines are seasonal variation of Ekman transport ($m^{-2}.s^{-1}$ per meter of coastline) for Core 1 and Core 2 over the period 2003–2015.

which impact surface waters in Core 2. This is reflected in the CUI standard deviation value which is 0.16 for Core 1 and 0.25 for Core 2. This analysis is again coherent with our results from the previous section which indicate a high annual variability found in Core 2. The CUI time series (Fig. 6) further shows that the seasonal cycles in the two cores are not in phase, with the maximum upwelling in Core 2 leading the maximum upwelling in Core 1 by one month. A significant linear relationship over the entire time series is found between the upwelling index and the chlorophyll A concentration for the two cores with a correlation of 0.72 for Core 2 and 0.58 for Core 1. These relationships confirm the link between surface cold water signature and nutrient enrichment through upwelling.

Compared to the upwelling cells of Senegal and Morocco, where similar upwelling indices were used, the upwelling in the coastal regions of south Madagascar index is relatively weak. In the upwelling of Senegal and Morocco, temperature differences between the offshore and coastal regions are at times greater than 5°C and result in an upwelling index in excess of 1 (Demarq and Faure, 2000; Benazzouz et al., 2014).

4. Mechanisms

4.1. Wind driven upwelling

The aim of this section is to identify the relationship between the CUI and wind forcing in each core. Cross Shore Ekman Transport (CSET) seasonal variations are calculated and plotted in Fig. 6. We note that the CSET is calculated using dominant angles of the coastline from true East (18.3° for Core 1, -30° for Core 2), according to the Eq. (3), for orienting the wind stress direction following the shape of coastline at each Core. For both cores, CSET seasonal variations present two periods of maximum (winter and late summer) and two periods of minimum (fall and early summer) throughout the year. The first distinct phase is the increase of local wind and upwelling intensity in winter. Fig. 6 shows that the CSET increases sharply from the beginning of winter (May) to late winter (September) for both cores. The upwelling indexes for both cores are also maximum in winter although they precede the maximum in cross-shelf Ekman transport. Another maximum of CSET is found in late summer (March) for both cores. This maximum is not as high as the winter peak and does not seem to be associated with a maximum in CUI (Fig. 6). The CSET decreases significantly twice in a year. An important decrease happens at the beginning of summer (October-November). This decrease is coherent with the reduction of upwelling intensity at the end of winter. Another decrease of CSET is observed between March and May. During this period the wind stress decreases abruptly while the CUI remains strong in both cores. Next, we examine how changes in the orientation of the coastline and predominant wind directions impact on the intensity of the SST derived upwelling index.

In Fig. 7, the south Madagascar coastline is smoothed to be able to extract the specific orientation of the different sections of the coastline. The sections are labeled “a” to “n”. We considered that the sections of coastline from “a to g” represent the Core 2 section, while the portions of coastline from “h to n” represent Core 1. The arrows indicate the mean wind direction in the upwelling region. Only wind speed and direction located over the shallow topography ($\leqslant$ 1000 m) are selected as potential drivers of upwelling wind-driven. We then compare the direction of the wind relative to the orientation of the coast for each portion of the smoothed coastline to explain the contribution of local wind to coastal upwelling intensity. In the wind roses depicted in Fig. 7, the blue lines represent the tangential orientation of each specific portion of coastline. The orientation of each coastline portion is compared with the dominant wind direction illustrated by the wind rose. The figure shows the correspondence between the dominant direction of the wind and the orientation tangent to the coastline. The results reveal that the orientation of the coastline in the south of Madagascar

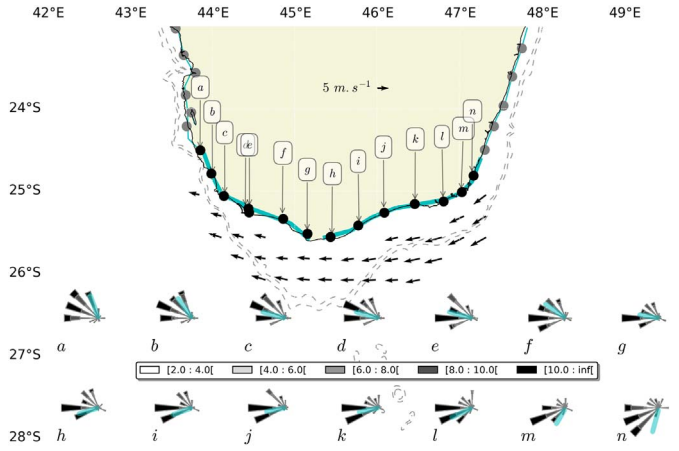

Fig. 7. In the map "a, b,…,n" are sections of the smoothed coastline represented by the solid turquoise line; Arrows are the average wind. Wind roses are polar distribution of wind intensities and directions for each section of coastline. The turquoise solid lines in the wind roses show the orientation of the smoothed coastline.

favours upwelling condition, especially for the sections "i, j, k, l" in Core 1 and "c, d, e, f, g" in Core 2, where the wind blows tangentially to the coastline. Fig. 7 shows that although the coastline presents a large curve, the wind is still mostly parallel to the coastline and therefore favorable to upwelling.

Fig. 8 shows the CSET calculated at different sections of coastline. The Hovmöller plot allows us to assess seasonal variations in the magnitude of the upwelling favorable winds. In agreement with Fig. 6, high values of CSET occur during two distinct periods. The CSET is large in late winter and moderate during summer for specific sections of the coastline. The results confirm that winds are upwelling favourable in late winter (Aug–Sep) for sections "i, j, k, l" (Core 1) and sections "c, d, e, f, g" (Core 2). In winter, the intensity of the CSET is similar for Core 1 and Core 2, in spite of a wind speed reduction of approximately $\backsim$ 3 m.s^{-1} from Core 1 towards Core 2. This is due to the more favourable orientation of the coastline for Core 2. In summer, the CSET is moderately intense at the beginning of the year and decreases in late summer for both cores. The results demonstrate that the local winds promote moderate upwelling in late summer and strong upwelling in late winter. However, the winds are not well correlated with the upwelling index for either cores.

To further investigate the contribution of the local wind in generating upwelling, we perform idealized numerical simulations. Fig. 9 shows that the annual mean SST from the reference simulation reproduces the coastal cold water representative of the upwelling. With weaker coastal winds, the upwelling signature is largely reduced, with SST up to 2°C warmer than in the reference experiment (Fig. 9b). However, a patch of colder SST can still be seen inshore of the EMC, showing that the upwelling in Core 1 is also influenced by the presence of the EMC. In Core 2, the upwelling signature vanishes in the idealized experiment, thereby illustrating the greater role played by the wind as a driver of upwelling for Core 2. This result confirms that the wind is not the only mechanism at play and the interactions of currents such as the EMC interaction with the continental shelf likely plays a significant role in driving the upwelling. Next, we look at the influence of EMC on upwelling intensity.

4.2. Influence of EMC on upwelling

Several authors have suggested that both the EMC and wind-driven upwelling act as drivers for the upwelling south of Madagascar (Lutjeharms and Machu, 2000; DiMarco et al., 2000; Ho et al., 2004). Fig. 10 presents monthly values of the upwelling index (CUI) in Core 1 and the volume transport (normalized by its standard deviation: 5.74 Sverdrups [1 SV = 10^6 m^3 s^{-1}]) of the EMC at 23°S, upstream of the coastal upwelling over the 2.5 years period of available in-situ current observations (Ponsoni et al., 2016). A monthly chlorophyll A concentration time series taken in Core 1 highlights the phytoplankton response to the current forcing. Despite the relative short period of the volume transport data (28 months), the correlation between the SST upwelling index and the EMC volume transport time series is significant at 95% with a Pearson's correlation coefficient equal to 0.59. This confirms the influence of the EMC on the upwelling and explains why upwelling in Core 1 might persist despite winds not being upwelling favorable throughout the year. Modulations in the EMC transport also appears be associated with variations of the Chlorophyll A concentration in Core 1 (correlation 0.28), although the seasonality shown in Fig. 6 results in a minimum around January while the EMC is still strong. A very low correlation value of 0.11 between the EMC volume transport time series and the SST upwelling index for Core 2 shows that the EMC is not a direct driver of seasonal variability in Core 2. A Lagrangian experiment to investigate the sources of upwelled water in each core is used to better understand the connectivity (or lack thereof) between Core 1 and Core 2.

4.3. Origin of upwelled water

To identify the major pathways for the upwelled water of each core, we advect virtual Lagrangian particles backwards in time using the outputs of the model simulation shown in Fig. 2. Fig. 11 shows the horizontal density and longitudinal distribution of the origin of the particles two months before the upwelling intensity peaks in winter. The green boxes are the locations where particles are released before backward advection. The density of particles that reach Core 2 in two months is higher along the west coast of Madagascar in the Mozambique Channel, between 19°S and 26°S. The large majority of the particles [81.69%] follow a coastal pathway along the west coast of Madagascar before reaching Core 2. A smaller proportion [18.31%] of particles that upwell in Core 2 arrive from the East, carried by the EMC. In contrast to Core 2, the particles upwelled in Core 1 arrive equally from both sides: 58.4% from the EMC and 41.6% from the Mozambique

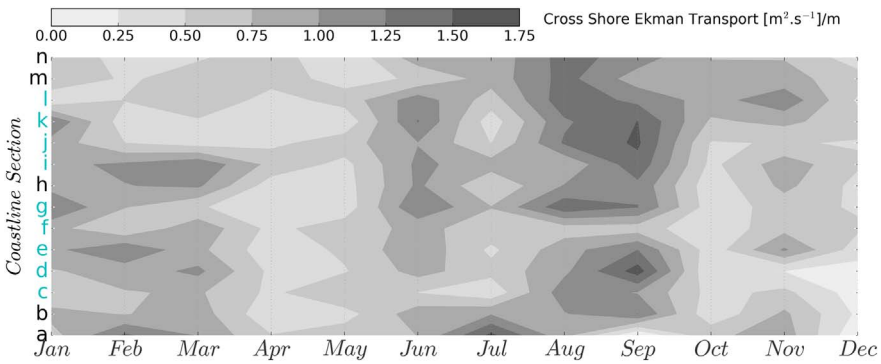

Fig. 8. Annual variation of Cross-shore Ekman transport (m^2.s^{-1} per meter of coastline) perpendicular to the coastline sections. Turquoise labels in y axis represent portions of coastline tangentially favourable for a wind-upwelling, where "i,j,k,l" for Core 1 and "c,d,e,f,g" for Core 2.

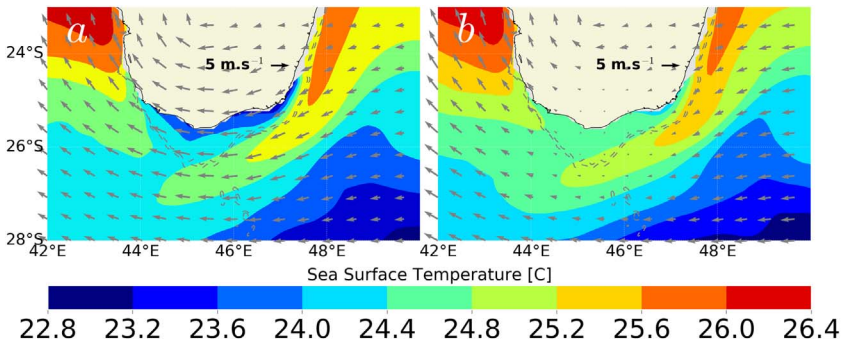

Fig. 9. Mean SST from (a) the reference simulation, overwritten by the wind surface (arrows), and (b) the simulation with an attenuation of the wind stress above the region of upwelling. Arrows show the mean surface wind used for the simulations.

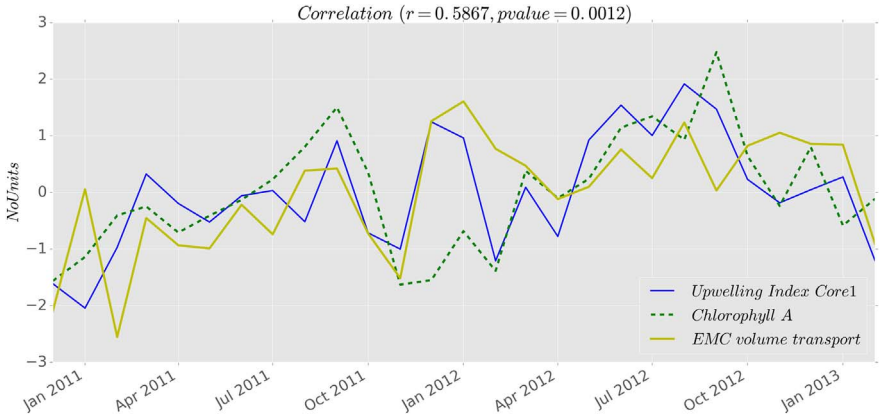

Fig. 10. Blue time series is the coastal upwelling index inside Core 1 (normalized); Yellow time series is the volume transport of East Madagascar Current (EMC) from ADCP transect located at 23°S (normalized). Green dash-dotted line is the chlorophyll A concentration inside Core 1 (normalized).

Channel. This shows that, although the EMC directly influences the upwelling in Core 1, it is not the only source of upwelled water.

5. Discussions and conclusion

Coastal upwelling south of Madagascar occurs predominantly in two well-defined upwelling cores. The first core (Core 1) is located in the southeastern corner of Madagascar, between the coastal zone and the EMC, while the second core (Core 2) is located west of the southern tip of Madagascar. The temporal behavior of these two cores is different. Upwelling in Core 1 is perennial throughout the year with a maximum toward the end of austral winter, while weak upwelling occurs in Core 2 from October to January. These differences arise from the difference in the drivers generating coastal upwelling. Our analyses, based on satellite observations and model simulations show that upwelling in Core 1 is forced concurrently by the EMC and the wind. The significant correlation between the upwelling index and the EMC flow confirms the influence of the EMC on Core 1, in agreement with Lutjeharms and Machu (2000) DiMarco et al. (2000) Ho et al. (2004). Ho et al. (2004) noted that the EMC strongly influences coastal upwelling along the southern Madagascan shores. Frontal variability in western boundary currents often leads to the formation of cyclonic eddies which can

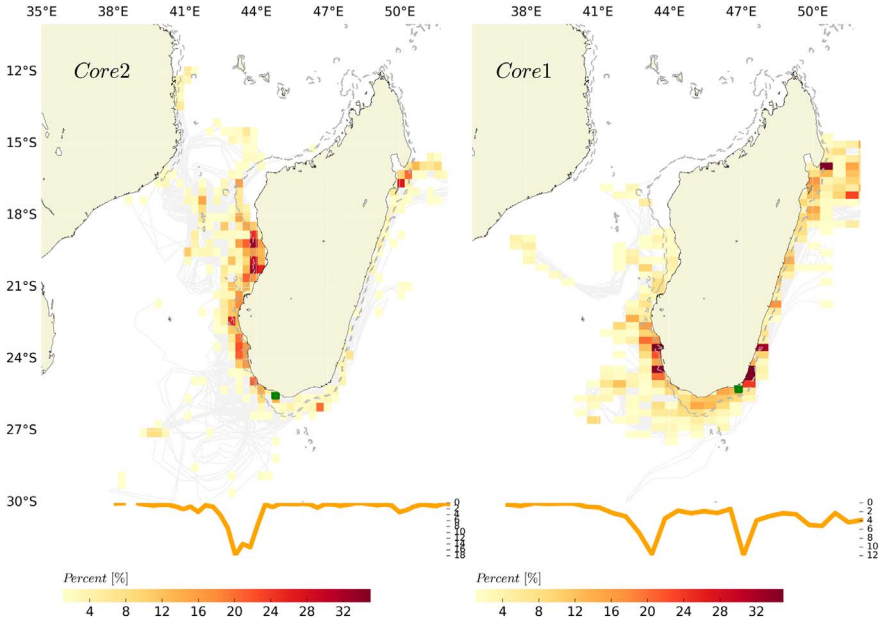

Fig. 11. (top) Spatial probability of water parcels origin 2 months before upwelling for Core 2 (left) and Core 1 (right) during the period of 2003 to 2013. (bottom) Latitudinal average of the probability density function of particle distribution. Green boxes are the areas covered by particles at the initial position.

contribute to the promotion of upwelling (Lee et al., 1991; Chia et al., 1982; Campos et al., 2000). The presence of such a cyclonic eddy and its potential role as a driver of upwelling was noted by Machu et al. (2002). In a recent work, Jose et al. (2016) used a coupled physical-biochemical model in the region and suppressed the momentum advection term in the Navier-Stokes equation. Jose et al. (2016) found that the coastal upwelling south of Madagascar disappears when the momentum advection (responsible for EMC detachment) is neglected in the model. Results from the model sensitivity study and the Ekman transport analysis show that the wind also drives upwelling in Core 1, in agreement with DiMarco et al. (2000). This dual forcing is confirmed through our Lagrangian analysis which shows that the water particles in Core 1 come from both the EMC and Mozambique Channel regions. A combination of the EMC and local wind forcing appears to be at the origin of the upwelling maximum observed in winter since the EMC is slightly more intense at this time of the year (Quartly and Srokosz, 2004; Voldsund, 2011) and the local wind is also stronger towards late winter/spring.

An upwelling front detection reveals a second distinct upwelling region (Core 2) west of the southern tip of Madagascar. In contrast with the upwelling in Core 1, the upwelling in Core 2 is not linked with the EMC. This results in a higher SST variability for Core 2 at seasonal and inter-annual time scales. Although local coastal winds are upwelling favorable for generating Core 2, the timing of the maximum in offshore Ekman transport does not match the upwelling index maximum. The lack of correlation between upwelling and local wind was also reported by Lutjeharms and Machu (2000). Since the upwelling in Core 2 is not directly linked with the EMC, there must be other drivers of upwelling variability in this region besides the winds. The Lagrangian analysis reveals the presence of a warm poleward flow along the west coast of Madagascar, which transports water particles from warm waters of the Mozambique Channel to Core 2. Such a warm poleward flow should result into a relatively deep thermocline along the southwestern shores of Madagascar. This is confirmed by cross sections in the realistic model simulation for each season, south-west of Madagascar (Fig. 12 left). In contrast with the section south-east of Madagascar, where the geostrophic balance across the EMC results in an uplift of the isotherms (Fig. 12 right), the poleward coastal flow is associated with a coastal deepening of the thermocline (represented here by the 22°C isotherm, Fig. 12 left). In this case, although winds are upwelling favorable, warm waters are upwelled, resulting in a weak upwelling signature in SST. This situation can be compared with the California upwelling system, where a deepening in the thermocline occurs during El-Nino events (Huyer and Smith, 1985). A large scale deepening of the thermocline associated with the poleward flow at the coast could be the reason why the intensity of the upwelling index becomes weaker during the summer in Core 2. DiMarco et al. (2000) have proposed that the summer upwelling is associated with the wind favorable upwelling. However, they did not exclude coastal circulation contributions.

In this study, we highlighted the presence of two separate upwelling cores south of Madagascar. The first core on the eastern side, inshore of the EMC, is associated with a dynamic upwelling driven by the detachment of the current, and upwelling favourable winds. The second core, more variable, is located west of the southern tip of Madagascar. While it is primarily forced by upwelling favourable winds, the intrusion of warm water from the Mozambique Channel may cause deviations from the seasonally wind driven upwelling cycle. The origin, nature and potential impact of warm water intrusions along the south-west shores of Madagascar are investigated in a follow-up paper to this study.

Acknowledgements

The authors want to thank UCT, the NRF SARCHi chair on Ocean Atmosphere Modelling, WRC, LMI ICEMASA, the Nansen Tutu Center for Marine Environmental Research for funding, and RAMI project, a regional doctoral school in the Indian Ocean zone, under the “Horizons Francophones” programme of the AUF (Agence Universitaire de la

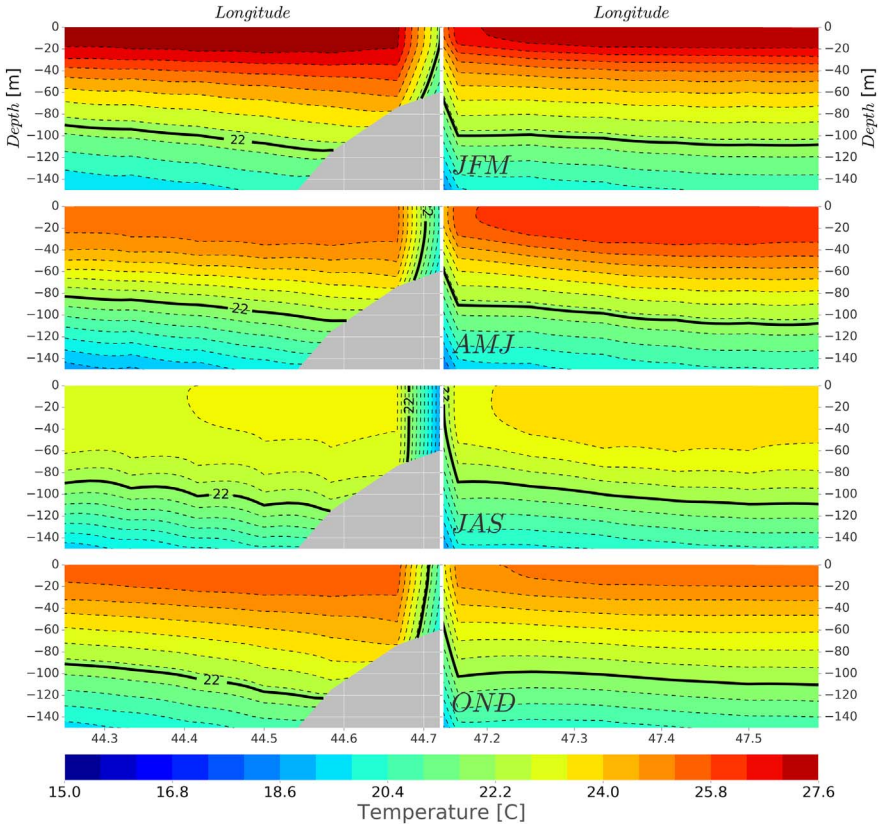

Fig. 12. Vertical sections of temperature taken along the transect plotted in Fig. 1.a. (Left) Seasonal variations of temperature close to Core 2. (Right) Seasonal variations of temperature close to Core 1. Bold lines represent 22°C of isotherms.

Francophonie). GlobCurrent products are available for free thanks to ESA funding under GlobCurrent DUE project AO/1-7472/13/I-LG. Numerical computations were performed on the IDRIS (Institut du Developpement et des Ressources en Informatique Scientifique) IBM "ADA" computer facility (grant A0020107630) and on the "CAPARMOR" computer facility at IFREMER, Brest. The authors are grateful to the two anonymous reviewers for their inputs that improved the quality of this work. At last we want to thanks Gigi who hosted us at Lavanono during our field trip South of Madagascar in June 2017.

References

Alvarez, I., Gomez-Gesteira, M., Lorenzo, M., Crespo, A., Dias, J., et al., 2011. Comparative analysis of upwelling influence between the western and northern coast of the Iberian Peninsula. Cont. Shelf Res. 31 (5), 388–399. http://dx.doi.org/10.1016/j.csr.2010.07.009.

Bakun, A., 1975. Daily and weekly upwelling indices, west coast of North America. NOAA Tech. Rpt 16. https://books.google.fr/books?id=D761PQAACAAJ.

Bemiasa, J., 2009. Dynamique des pêcheries traditionnelles dŠanchois, de calmars et de poulpes du Sud-Ouest de Madagascar: utilisation dŠoutils océanographiques pour la gestion des ressources. Ph.D. thesis. Universite de Toliara, Madagascar. http://archimer.ifremer.fr/doc/2009/these-6847.pdf.

Benazzouz, A., Mordane, S., Orbi, A., Chagdali, M., Hilmi, K., Atillah, A., Pelegrí, J.L., Hervé, D., 2014. An improved coastal upwelling index from sea surface temperature using satellite-based approach-the case of the Canary Current upwelling system. Cont. Shelf Res. 81, 38–54. http://dx.doi.org/10.1016/j.csr.2014.03.012.

Campos, E.J., Velhote, D., da Silveira, I.C., 2000. Shelf break upwelling driven by Brazil current cyclonic meanders. Geophys. Res. Lett. 27 (6), 751–754. http://dx.doi.org/10.1029/1999GL010502.

Canny, J., 1986. A computational approach to edge detection. IEEE Trans. Pattern Anal. Mach. Intell. (6), 679–698. http://dx.doi.org/10.1109/TPAMI.1986.4767851.

Chia, F., Griffiths, R., Linden, P., 1982. Laboratory experiments on fronts: part II: the formation of cyclonic eddies at upwelling fronts. Geophys. Astrophys. Fluid Dyn. 19 (3-4), 189–206. http://dx.doi.org/10.1080/03091928208208955.

Conkright, M.E., Locarnini, R.A., Garcia, H.E., O'Brien, T.D., Boyer, T.P., Stephens, C., Antonov, J.I., 2002. World Ocean Atlas 2001: Objective Analyses, Data Statistics, and Figures: CD-ROM Documentation. US Department of Commerce, National Oceanic and Atmospheric Administration, National Oceanographic Data Center, Ocean Climate Laboratory.

Debreu, L., Marchesiello, P., Penven, P., Cambon, G., 2012. Two-way nesting in split-explicit ocean models: algorithms, implementation and validation. Ocean Model. 49, 1–21. http://dx.doi.org/10.1016/j.ocemod.2012.03.003.

Dee, D., Uppala, S., Simmons, A., Berrisford, P., Poli, P., Kobayashi, S., Andrae, U., Balmaseda, M., Balsamo, G., Bauer, P., et al., 2011. The ERA-Interim reanalysis: configuration and performance of the data assimilation system. Q. J. R. Meteorol. Soc. 137 (656), 553–597. http://dx.doi.org/10.1002/qj.828.

Demarq, H., Faure, V., 2000. Coastal upwelling and associated retention indices derived from satellite sst. application to octopus vulgaris recruitment. Oceanol. Acta 23 (4), 391–408. http://dx.doi.org/10.1016/S0399-1784(00)01113-0.

DiMarco, S.F., Chapman, P., Nowlin, W.D., 2000. Satellite observations of upwelling on the continental shelf south of Madagascar. Geophys. Res. Lett. 27 (24), 3965–3968. http://dx.doi.org/10.1029/2000GL012012.

Fairall, C.W., Bradley, E.F., Rogers, D.P., Edson, J.B., Young, G.S., 1996. Bulk parameterization of air-sea fluxes for tropical ocean-global atmosphere coupled-ocean atmosphere response experiment. J. Geophys. Res. Oceans 101 (C2), 3747–3764. http://dx.doi.org/10.1029/95JC03205.

Ferry, N., Parent, L., Garric, G., Bricaud, C., Testut, C., Le Galloudec, O., Lellouche, J., Drévillon, M., Greiner, E., Barnier, B., et al., 2012. Glorys2v1 global ocean reanalysis of the altimetric era (1992–2009) at meso-scale. Mercator quarterly newsletter 44, January 2012, 29-39.

Gonzalez-Nuevo, G., Gago, J., Cabanas, J., 2014. Upwelling index: a powerful tool for marine research in the NW Iberian upwelling system. J. Oper. Oceanography 7 (1), 47–57. http://dx.doi.org/10.1080/1755876X.2014.11020152.

Gula, J., Molemaker, M.J., McWilliams, J.C., 2014. Submesoscale cold filaments in the Gulf Stream. J. Phys. Oceanogr. 44 (10), 2617–2643. http://dx.doi.org/10.1175/JPO-D-14-0029.1.

Gunther, E., 1936. A report on oceanographic investigations in the Peru coastal current, discovery reports, 13, 107-276.

Halo, I., Backeberg, B., Penven, P., Ansorge, I., Reason, C., Ullgren, J., 2014. Eddy properties in the Mozambique Channel: a comparison between observations and two numerical ocean circulation models. Deep-Sea Res. II Top. Stud. Oceanogr. 100, 38–53. http://dx.doi.org/10.1016/j.dsr2.2013.10.015.

Hasager, C.B., Mouche, A., Badger, M., Bingöl, F., Karagali, I., Driesenaar, T., Stoffelen, A., Peña, A., Longépé, N., 2015. Offshore wind climatology based on synergetic use of Envisat ASAR, ASCAT and QuikSCAT. Remote Sens. Environ. 156, 247–263. http://dx.doi.org/10.1016/j.rse.2014.09.030.

Higdon, D., 1998. A process-convolution approach to modelling temperatures in the North Atlantic Ocean. Environ. Ecol. Stat. 5 (2), 173–190. http://dx.doi.org/10.1023/A:1009666805688.

Hilburn, K., Wentz, F., Smith, D., Ashcroft, P., 2006. Correcting active scatterometer data for the effects of rain using passive radiometer data. J. Appl. Meteorol. Climatol. 45 (3), 382–398. http://dx.doi.org/10.1175/JAM2357.1.

Ho, C.-R., Zheng, Q., Kuo, N.-J., 2004. SeaWiFs observations of upwelling south of Madagascar: long-term variability and interaction with East Madagascar Current. Deep-Sea Res. II Top. Stud. Oceanogr. 51 (1), 59–67. http://dx.doi.org/10.1016/j.dsr2.2003.05.001.

Houart, R., Héros, V., 2013. Description of new Muricidae (Mollusca: Gastropoda) collected during the ATIMO VATAE expedition to Madagascar "Deep South". Zoosystema 35 (4), 503–523. http://dx.doi.org/10.5252/z2013n4a5.

Huhn, F., Kameke, A., Pérez-Muñuzuri, V., Olascoaga, M., Beron-Vera, F., 2012. The impact of advective transport by the south Indian Ocean countercurrent on the Madagascar plankton bloom. Geophys. Res. Lett. 39 (6).

Huyer, A., Smith, R.L., 1985. The signature of El Nino off Oregon, 1982–1983. J. Geophys. Res. Oceans 90 (C4), 7133–7142. http://dx.doi.org/10.1029/JC090iC04p07133.

Johannessen, J., Chapron, B., Collard, F., Rio, M., Piollé, J., Quartly, G., Shutler, J., Donlon, C., Danielson, R., Korosov, A., et al., 2015. Globcurrent: Sentinel-3 synergy in action. In: Proceedings of Sentinel-3 for Science Workshop (2-5 June 2015, Venice, Italy). ESA. http://adsabs.harvard.edu/abs/2015ESASP.734.2J.

Jose, Y.S., Penven, P., Aumont, O., Machu, E., Moloney, C., Shillington, F., Maury, O., 2016. Suppressing and enhancing effects of mesoscale dynamics on biological production in the Mozambique Channel. J. Mar. Syst. 158, 129–139. http://dx.doi.org/10.1016/j.jmarsys.2016.02.003.

Large, W., Pond, S., 1981. Open ocean momentum flux measurements in moderate to strong winds. J. Phys. Oceanogr. 11 (3), 324–336. http://dx.doi.org/10.1175/1520-0485(1981)011<0324:OOMFMI>2.0.CO;2.

Lee, T.N., Yoder, J.A., Atkinson, L.P., 1991. Gulf stream frontal eddy influence on productivity of the southeast US continental shelf. J. Geophys. Res. Oceans 96 (C12), 22191–22205. http://dx.doi.org/10.1029/91JC02450.

Longhurst, A., 2001. A major seasonal phytoplankton bloom in the Madagascar basin. Deep-Sea Res. I Oceanogr. Res. Pap. 48 (11), 2413–2422. http://dx.doi.org/10.1016/S0967-0637(01)00024-3.

Lutjeharms, J., Machu, E., 2000. An upwelling cell inshore of the East Madagascar Current. Deep-Sea Res. I Oceanogr. Res. Pap. 47 (12), 2405–2411. http://dx.doi.org/10.1016/S0967-0637(00)00026-1.

Machu, E., Lutjeharms, J., Webb, A., Van Aken, H., 2002. First hydrographic evidence of the southeast Madagascar upwelling cell. Geophys. Res. Lett. 29 (21). http://dx.doi.org/10.1029/2002GL015381.

Oram, J.J., McWilliams, J.C., Stolzenbach, K.D., 2008. Gradient-based edge detection and feature classification of sea-surface images of the southern California bight. Remote Sens. Environ. 112 (5), 2397–2415. http://dx.doi.org/10.1016/j.rse.2007.11.010.

Othman, Z., Abdullah, A., Prabuwono, A.S., 2012. A statistical approach of multiple resolution levels for canny edge detection. In: Intelligent Systems Design and Applications (ISDA), 2012 12th International Conference on. IEEE, pp. 837–841. http://dx.doi.org/10.1109/ISDA.2012.6416646.

Ping, B., Su, F., Meng, Y., Du, Y., Fang, S., 2016. Application of a sea surface temperature front composite algorithm in the Bohai, Yellow, and East China Seas. Chin. J. Oceanol. Limnol. 34, 597–607. http://dx.doi.org/10.1007/s00343-015-4356-7.

Ponsoni, L., Aguiar-González, B., Ridderinkhof, H., Maas, L.R., 2016. The East Madagascar Current: volume transport and variability based on long-term observations. J. Phys. Oceanogr. 46 (4), 1045–1065. http://dx.doi.org/10.1175/JPO-D-15-0154.1.

Pripp, T., Gammelsrød, T., Krakstad, J., 2014. Physical influence on biological production along the western shelf of Madagascar. Deep-Sea Res. II Top. Stud. Oceanogr. 100, 174–183. http://dx.doi.org/10.1016/j.dsr2.2013.10.025.

Quartly, G., Srokosz, M., 2004. Following the fate of the East Madagascar Current.

Raj, R.P., Peter, B.N., Pushpadas, D., 2010. Oceanic and atmospheric influences on the variability of phytoplankton bloom in the southwestern Indian ocean. J. Mar. Syst. 82 (4), 217–229. http://dx.doi.org/10.1016/j.jmarsys.2010.05.009.

Rakotoarinivo, A.W., 1998. Les petits poissons pélagiques de la région de Toliara Sud Ouest de Madagascar: biologie, écologie, exploitation et aménagement. Ph.D. thesis. Université de Toliara. http://hdl.handle.net/1834/9456.

Shchepetkin, A.F., McWilliams, J.C., 2005. The regional oceanic modeling system (ROMS): a split-explicit, free-surface, topography-following-coordinate oceanic model. Ocean Model. 9 (4), 347–404. http://dx.doi.org/10.1016/j.ocemod.2004.08.002.

Siedler, G., Rouault, M., Biastoch, A., Backeberg, B., Reason, C.J., Lutjeharms, J.R., 2009. Modes of the southern extension of the east Madagascar current. J. Geophys. Res. Oceans 114 (C1). http://dx.doi.org/10.1029/2008JC004921.

Simhadri, K.K., Iyengar, S., Holyer, R.J., Lybanon, M., Zachary, J.M., 1998. Wavelet-based feature extraction from oceanographic images. IEEE Trans. Geosci. Remote Sens. 36 (3), 767–778. http://dx.doi.org/10.1109/36.673670.

Srokosz, M., Quartly, G., 2013. The Madagascar bloom: a serendipitous study. J. Geophys. Res. Oceans 118 (1), 14–25. http://dx.doi.org/10.1029/2012JC008339.

Srokosz, M., Robinson, J., McGrain, H., Popova, E., Yool, A., 2015. Could the madagascar bloom be fertilized by Madagascan iron? J. Geophys. Res. Oceans 120 (8), 5790–5803. http://dx.doi.org/10.1002/2015JC011075.

Vazquez-Cuervo, J., Dewitte, B., Chin, T.M., Armstrong, E.M., Purca, S., Alburqueque, E., 2013. An analysis of SST gradients off the Peruvian Coast: the impact of going to higher resolution. Remote Sens. Environ. 131, 76–84. http://dx.doi.org/10.1016/j.rse.2012.12.010.

Veitch, J., Penven, P., Shillington, F., 2010. Modeling equilibrium dynamics of the Benguela current system. J. Phys. Oceanogr. 40 (9), 1942–1964. http://dx.doi.org/10.1175/2010JPO4382.1.

Voldsund, A., 2011. The Dynamics of the East Madagascar Current System and Its Influence on the Biological Production Associated to the Shelf-An Observational Study. Master's thesis. The University of Bergen. http://hdl.handle.net/1956/5198.

Wilson, C., Qiu, X., 2008. Global distribution of summer chlorophyll blooms in the oligotrophic gyres. Prog. Oceanogr. 78 (2), 107–134. http://dx.doi.org/10.1016/j.pocean.2008.05.002.